Soft Matter

Accepted Manuscript

ROYAL SOCIETY OF CHEMISTRY

www.rsc.org/softmatter

Journal Name

ARTICLE TYPE

Cite this: DOI: 10.1039/xxxxxxxxxx

A Microscopic Gibbs field model for the macroscopic yielding behaviour of a viscoplastic fluid†

Raazesh Sainudiin,[a] Miguel Moyers-Gonzalez,[a] and Teodor Burghelea[b]‡

Received Date
Accepted Date

DOI: 10.1039/xxxxxxxxxx

www.rsc.org/journalname

We present a Gibbs random field model for the microscopic interactions in a viscoplastic fluid. The model has only two parameters which are sufficient to describe the internal energy of the material in the absence of external stress and a third parameter for a constant externally applied stress. The energy function is derived from the Gibbs potential in terms of the external stress and internal energy. The resulting Gibbs distribution, over a configuration space of microscopic interactions, can mimic experimentally observed macroscopic behavioural phenomena that depend on the externally applied stress. A simulation algorithm that can be used to approximate samples from the Gibbs distribution is given and it is used to gain several insights about the model. Corresponding to weak interactions between the microscopic solid units, our model reveals a smooth solid-fluid transition which is fully reversible upon increasing/decreasing external stresses. If the interaction between neighbouring microscopic constituents exceeds a critical threshold the solid-fluid transition becomes abrupt and a hysteresis of the deformation states is observed even at the asymptotic limit of steady forcing. Quite remarkably, in spite of the limited number of parameters involved, the predictions of our model are in a good qualitative agreement with macro rheological experimental results on the solid-fluid transition in various yield stress materials subjected to an external stress.

1 Introduction

Yield stress materials or *viscoplastic fluids* are ubiquitous in nature and they are encountered daily in a variety of forms: foods (mayonnaise, molten chocolate, mustard, ketchup), cosmetic products (shaving foam, tooth paste, hair gel, shampoos, hand and face creams), drilling muds, cements, volcanic lava, molten metals, suspensions of microalgae etc. A particular class of yield stress materials is the *physical gel*. Due to their large water content, the physical gels are compatible with biological tissues which makes them excellent candidates for various biomedical applications: targeted drug delivery[1,2], contact lenses, noninvasive intervertebral disc repair[3] and tissue engineering[4].

From a mechanical perspective, such materials behave as solids if the stresses applied onto them are smaller than a threshold value σ_y generally referred to as the "yield stress", and as fluids otherwise.

It is widely believed that the macroscopic yield stress behaviour originates from the presence of a microstructure which can sustain a finite local stress prior to breaking apart and allowing for a macroscopic flow to set in.

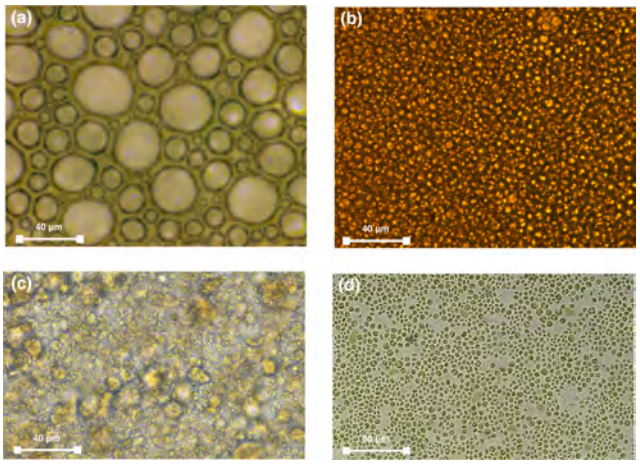

Fig. 1 Micrographs of several yield stress materials: **(a)** commercial shaving gel (Gillette Series) **(b)** mayonnaise (Carrefour, France) **(c)** 5% bentonite in water **(d)** suspension of Chlorella Vulgaris unicellular micro alga (reproduced from Ref.[5]).

To illustrate this, we present in Fig. 1 micrographs (acquired in

[a] *School of Mathematics and Statistics, Private Bag 4800, University of Canterbury, Christchurch 8041, New Zealand*
[b] *Université de Nantes, Nantes Atlantique Universités, CNRS, Laboratoire de Thermocinétique de Nantes, UMR 6607, La Chantrerie, Rue Christian Pauc, B.P. 50609, F-44306 Nantes Cedex 3, France; E-mail: teodor.burghelea@univ-nantes.fr*
† Electronic Supplementary Information (ESI) available: [details of any supplementary information available should be included here]. See DOI: 10.1039/b000000x/
‡ Corresponding author.

a quiescent state) of several materials that exhibit a yield stress behaviour. In spite of clear differences in the chemical nature (and, consequently, physico-chemical properties) of these materials, heterogeneous and soft-solid like aggregates are visible in each of the micrographs presented in Fig. 1. A microscopic experimental study of the yielding would require monitoring in real time both the motion of such aggregates and the dynamics of their break-up (and, possibly, reforming) during flow. This experimental approach is difficult to implement and we are aware of only one previous work that describe the evolution of the microstructure during yielding [6].

The solid-fluid transition may be investigated during macroscopic rheological experiments by subjecting the material to a controlled stress ramp and monitoring its response (the rate of shear $\dot{\gamma}$). Prior to yielding negligibly small shear rates are measured whereas above the yield point non-zero values are recorded which allows one to *"guess"* the yield point.

We illustrate such measurements performed on a controlled stress rheometer (Mars III from Thermo Fischer Scientific) equipped with a serrated plate - plate geometry with three chemically and micro-structurally distinct yield stress materials (a commercially available mayonnaise, a commercially available mustard and an aqueous Carbopol gel very similar to the commercially available hair gels) in Fig. 2.

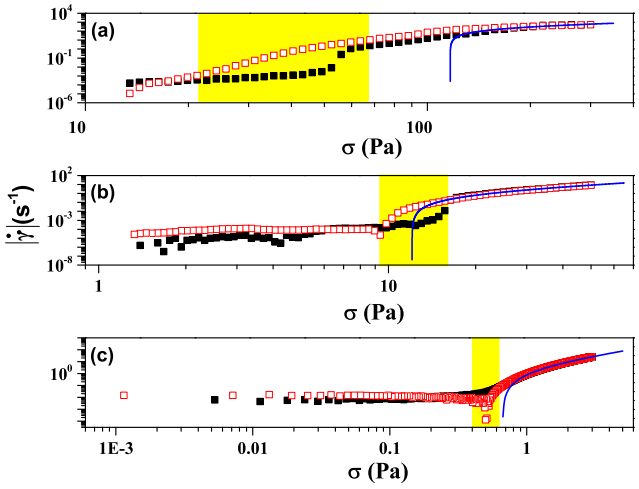

Fig. 2 Rheological flow curves measured via controlled stress ramps for various materials: **(a)** mayonnaise (Carrefour, France) **(b)** mustard (Carrefour, France) **(c)** 0.08% (wt) aqueous solution of Carbopol 980. The full/empty symbols in each panels refer to the increasing/decreasing branches of the stress ramp. For each stress value the response of the material was averaged during $t_0 = 10s$. The range of applied stresses corresponding to the yielding transition is highlighted in each subplot. The full lines are non linear fitting functions according to the Herschel-Bulkley model.

The data presented in Fig. 2 has been acquired during controlled stress ramps performed for both increasing and decreasing stresses. Corresponding to each applied stress, the response of the material (the rate of shear $\dot{\gamma}$) has been recorded during a finite time, $t_0 = 10\ s$.

The macroscopic yielding behaviour observed during experiments similar to the ones illustrated in Fig. 2 is often modelled by the Herschel-Bulkley law [7,8], $\sigma = \sigma_y + K\dot{\gamma}^N$. Here $\dot{\gamma}$ is the rate of shear, i.e., the rate at which the material is being deformed, σ is the externally applied stress to cause this deformation, K is a so-called consistency parameter that sets the viscosity scale in the flowing state and N is the power law index which characterizes the degree of shear thinning of the viscosity beyond the yield point. In the particular case of a Newtonian behaviour beyond the yield point with $N = 1$, this model reduces to the Bingham model [9].

In spite of its wide use by rheologists, fluid dynamicists, applied mathematicians and engineers, the Herschel-Bulkley model (and its regularized variants, e.g. Papanastasiou [10]) is in fact applicable only for a limited number of yield stress materials, sufficiently far from the solid-fluid transition, i.e. when $\sigma > \sigma_y$, and in the conditions of a steady state forcing, i.e. when a constant external stress σ is applied over a very long period of time ($t_0 \to \infty$). For each material investigated in Fig. 2 a departure from the Herschel-Bulkley yielding scenario is clearly visible within the transitional regime (the highlighted parts in each panel) - see the full lines. The data presented in Fig. 2 indicate that the solid-fluid transition is gradual: the material does not yield at a given value σ_y of the applied stress but within a finite interval of stresses (see the highlighted regions in Fig. 2).

Thixotropy, which may be loosely understood as a time dependence of the microstructure (and, implicitly, of the macroscopic rheological parameters) results from a competition between destruction and rejuvenation of the soft material units subjected to stress and is a major reason for the departure from this simple yielding scenario [11]. During controlled stress ramps performed for both increasing and decreasing stresses the thixotropy manifests through the emergence of a rheological hysteresis which is consistent with an irreversibility of the deformation states. This effect is visible in each of the panels (a-c) of Fig. 2 but its magnitude is clearly related to the specific microstructure of each material.

We present in Fig. 3 the dependence of the magnitude of the rheological hysteresis on the characteristic time t_0 for each of the materials characterised in Fig. 2.

For the case of mayonnaise and mustard (the circles and the squares in Fig. 3), a non monotone dependence of the magnitude of the hysteresis on the characteristic forcing time t_0 is observed. Corresponding to low values of t_0 (fast forcing) the hysteresis area first increases and then, for large values of t_0 (slow forcing), decreases following a power law. This non monotone behaviour agrees well with the measurements of Divoux and his coworkers performed for several yield stress materials: mayonnaise, laponite gel and carbon black gel, [12]. As pointed out in [12], these non monotone dependencies may be fitted by a log normal function (the dashed lines in Fig. 3). The presence of a local maximum of these curves has been attributed to the existence of a critical time scale $t_0^\star$ specific to each material which describes the restructuration dynamics of the solid material units. Thus, it was suggested that this non monotone behaviour is universal and can be observed for any pasty material.

It has been shown recently that a clear departure from the Herschel-Bulkley behaviour can be observed even for "*simple*" yield stress fluids such as the Carbopol gels particularly during un-

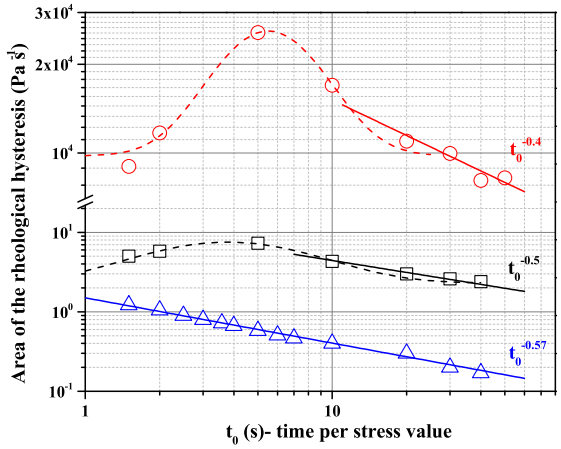

Fig. 3 Dependence of the hysteresis area on the characteristic forcing time t_0 (see text for description) measured with several yield stress materials via controlled-stress flow ramps: circle (○) - mayonnaise (Carrefour, France), square (□) - mustard (Carrefour, France), up triangle (△) - 0.08% (wt) aqueous solution of Carbopol 980. The dashed lines are log-normal fitting functions (see text for the discussion), the full lines are power law fitting functions indicated in the inserts.

steady flows taking place around the yield point[12–15]. The yielding behaviour of a Carbopol gel is illustrated here in panel (c) of Fig. 2. As compared to the mayonnaise and the mustard, no local maximum was observed in the dependence of the hysteresis area on the characteristic forcing time. It is suggested in Ref. [12] that in the case of a Carbopol gel the maximum may occur at values of t_0 which are too small to probe during rheologic tests. ~~but a~~ A negative power law scaling is observed for large t_0 which indicates that in the limit of very slow forcing ~~(large t_0)~~ the Carbopol gels behave as non-thixotropic yield stress fluids.

To overcome the difficulties in capturing the underlying physics of yielding via rheological tests, several phenomenological macroscopic models have been proposed[13,16–22]. The common feature of these models is the quantity $\bar{a}(t)$, the volume fraction of the unyielded material at time t whose time evolution is directly related to the applied stress via an evolution equation in the form $\frac{d\bar{a}(t)}{dt} = F[\bar{a}(t), \sigma(t)]$. Thus, as the applied stress is increased, $\bar{a}(t)$ varies smoothly from 1 to 0 and the combined solid and fluid rheological responses are weighted accordingly into a constitutive relation.

As opposed to the Bingham and the Herschel-Bulkley models which predict an abrupt solid-fluid transition when $\bar{a}$ jumps from 1 to 0 (this can be indirectly inferred from Fig. 2 by monitoring the full lines) at a well defined value of the applied stress, say, $\sigma = \sigma_y$, such approaches which directly account for the evolution of $\bar{a}(t)$ are able to describe several features observed in macroscopic experiments (which we have partially illustrated in Fig. 2), such as:

1. a smooth (gradual) solid-fluid transition as opposed to a sharp transition observed at a well defined value of the applied stress σ_y.
2. the irreversibility of the deformation states upon increasing/decreasing applied stresses that is implied by the observation of a hysteresis of the deformation states.
3. a clear dependence of the yielding/gelating scenario, as reflected by the area of the hysteresis, on the degree of the steadiness of the external forcing, i.e. how fast is the external stress varied during the solid-fluid transition, see Fig. 3 and Refs.[13,15] for a comprehensive discussion.

Though able to model sufficiently complex rheological data (ranging from controlled stress/strain unsteady flow ramps, creep tests and oscillatory tests in a wide range of frequencies and amplitudes), such phenomenological macroscopic models do have a number of limitations. First, they typically involve a rather large number of parameters which are not directly and easily measurable and can be obtained only by fitting the experimental data. Second, such models are not inherently validated from a thermodynamical standpoint — the second law of thermodynamics is not guaranteed to be held — and such a validation is not always straightforward as it requires the derivation of a thermodynamic potential[23,24]. Third, although able to describe rheological data similar to those presented in Fig. 2, such models are unable to provide insights into the microscopic scale dynamics of the solid-fluid transition because they solely describe a macroscopic volume fraction $\bar{a}(t)$ but not the evolution of the microscopic solid-fluid interfaces.

Because the macroscopic yield stress behaviour exemplified in Fig. 2 originates from the presence of a "soft" microstructure, an alternative way of assessing the dynamics of the yielding process is to focus on the evolution of the micro-structural soft material units (or aggregates) as the external stress is gradually increased past the solid-fluid transition and ~~next to~~ thereby assess the macroscopic scale behaviour from the perspective of statistical mechanics.

There exist only few theoretical and/or experimental studies focusing on the microscopic scale description of the macroscopic yielding (a deformative transformation of solid to fluid under an increasing stress regime) *and* the macroscopic gelation (a constitutive transformation of liquid to solid under a decreasing stress regime) of physical gels. This sets the main scope of the present contribution.

A thermodynamic approach for the deformation of a physical gel has been recently proposed by An and coworkers[25]. By using a mean field approach, they construct a free energy functional and describe the microscopic scale dynamics of the gel network as a function of the applied stress in terms of the monomer volume fraction and an internal connectivity tensor characterizing the gel network. As the free energy functional they propose accounts for the elastic energy, the mixing energy and the bond energy, the approach of An and coworkers is quite general and is expected to be applicable to a broad class of physical gels and chemical gels with a fixed number of monomers per cross-link.

De Bruyn has modelled the restricted diffusion of small tracer particles in heterogeneous media by performing Monte Carlo simulations in ~~a~~ an uncorrelated site-percolation model[26]. His simulations reveal a transition from a viscous to an elastic behaviour at a site-filling probability that is different from that corresponding to the percolation transition. He explains this finding by the

confinement of the tracers in the spatially heterogeneous medium which makes the general Stokes-Einstein relation inapplicable in this case. A partial agreement between the results of the simulation and experimental results is found[27,28].

We propose in the following a microscopic model for the yielding or gelation, corresponding to $\bar{a}$ approaching 0 or 1 respectively, of a physical gel using an essentially bi-parametric family of a correlated site percolation ~~that is inspired by the two dimensional Ising~~ model [37] that extends the uncorrelated version [26] towards a correlated version [33] but with an emphasis on the effects of externally applied and time-varying stress ramps. Our model builds on the analogy between the local agglomerative interactions in terms of assembly/disassembly of neighbouring gel particles in a microscopic gel network — see[31] (2.5,2.6,5.9,5.9.1,5.9.1.1,8.1.4) and[32] for standardized nomenclature — subjected to an external stress field.

~~By the analogy with the Ising model for the ferromagnetism w~~ We are placing the problem of yielding of a soft solid under stress in the more general context of "*Phase Transitions and Critical Phenomena*" and fully benefit from a number of theoretical tools developed during the past five decades and the computational power readily available for gaining physical insights into the solid-fluid transition.

Our thermodynamically consistent microscopic model with only two parameters that reflect the rheological properties of the gel and only two energy-determining configuration statistics — the number of gelled particles and the number of gelled pairs of neighboring particles — is able to capture the macroscopic behaviours of yielding and gelation for any stress regime given as a function of time, including hysteretic effects, if any. Our approach is fundamentally probabilistic and formalizes Gibbs fields as time-homogeneous and time-inhomogeneous Markov chains over the state space of all microscopic configurations.

The paper is organized as follows. The mathematical formulation of the model and the simulation algorithm are presented in Sec. 2 with details in the Appendix. The results of the simulations according to the microscopic model are presented in Sec. 3. The paper concludes in Sec. 4 with a discussion of the main findings and their possible implications and extensions.

2 Model

Let us model an idealized yield stress material or viscoplastic fluid as a network of microscopic constituents in an appropriate solvent that are capable of assembling by "forming bonds" or disassembling by "breaking bonds" with their neighbors. Without making any assumption about either the nature of the bonds or the physical nature of the interactions among neighbouring microscopic constituents, we investigate the model when the network of particles is the regular graph given by the toroidal two-dimensional square lattice as illustrated in Fig. 4 and the bonds/interactions are accounted for in a generic manner as detailed in the following.

Let the set of nodes or sites be

$$\mathbb{S}_n = \{1,2,\ldots,n\}^2 = \{(1,1),(1,2),\ldots,\ldots,(n,n)\} \ .$$

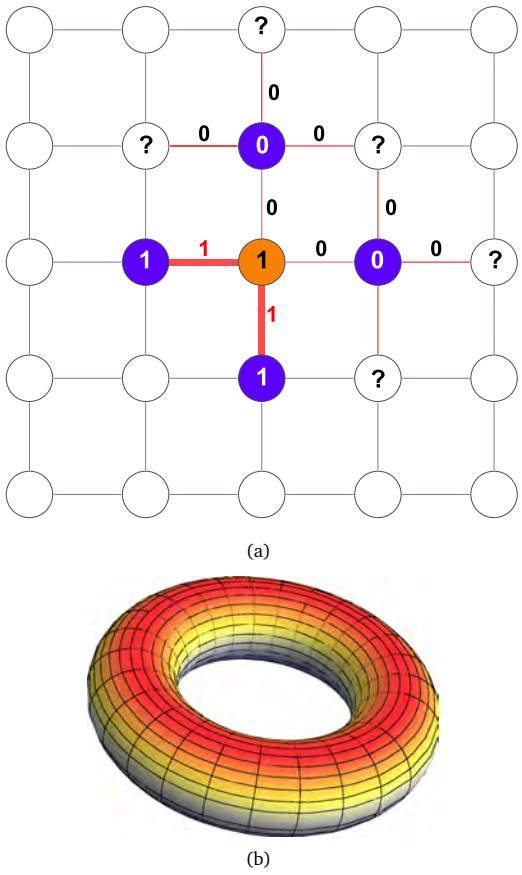

(a)

(b)

Fig. 4 (a) The regular graph represented for $n = 5$. The vertices labeled with $1/0$ represent microgel particles in a *unyielded*/*yielded* state, respectively. The labels $1/0$ of the edges indicate indicate whether two sites are *connected*/*unconnected*. (b) $2D$ toroidal lattice suggesting the periodic boundary conditions used through the simulations.

Let $N_s = \{r : \|\overline{(r-s)}_n\| = 1\}$ denote the set of four nearest neighboring sites of a given site $s \in \mathbb{S}_n$, where $\overline{(r-s)}_n$ denotes coordinate-wise subtraction modulo n and $\|\cdot\|$ denotes the Euclidean distance. Then the set of edges between pairs of sites is

$$\mathbb{E}_n = \bigcup_{s\in\mathbb{S}_n} \{\langle s,r\rangle : r \in N_s\} \subset \mathbb{S}_n^2 \ .$$

Let $|A|$ denote the size of the set A. Note that $|\mathbb{S}_n| = n^2$ and $|\mathbb{E}_n| = 2n^2$. Each site $s \in \mathbb{S}_n$ can be thought to represent a microscopic *clump* of particles in a particular region of the material and each edge $\langle s,r\rangle \in \mathbb{E}_n$ represents a potential *connection* between neighboring clumps at sites s and r. At the finest resolution of the model, each site can be a monomer molecule in the material and each edge can represent a potential bond between neighboring molecules. Let $x_s \in \Lambda = \{0,1\}$ denote the phase at site s. Phase 0 corresponds to being *yielded* or *ungelled* and phase 1 corresponds to being *unyielded* or *gelled*. The phase at a site directly affects its *connectability* with its neighboring sites. We assume that only two gelled sites can be connected with one another. Thus, the

connectivity between sites s and r is given by

$$y_{\langle s,r\rangle} = \begin{cases} 1 & \text{if } r \in N_s \text{ and } x_r x_s = 1 \\ 0 & \text{otherwise.} \end{cases} \quad (1)$$

In other words, we say that sites s and r are *connected*, i.e., $y_{\langle s,r\rangle} = 1$, if and only if $x_s = x_r = 1$ and s and r are neighbors. Otherwise, we say s and r are *unconnected*, i.e., $y_{\langle s,r\rangle} = 0$. These definitions are schematically illustrated in Fig. 4(a). Since the phase of sites determine their connectedness, we refer to sites in phase 1 as *connectable* and those in phase 0 as *unconnectable*. Thus, every site configuration $x \in \mathbb{X}_n := \Lambda^{\mathbb{S}_n}$ has an associated *edge configuration* $y \in \mathbb{Y}_n := \Lambda^{\mathbb{E}_n}$ which characterizes the connectivity information between all pairs of neighboring sites. We use X to denote a *random site configuration* and $Y = Y(X)$ to denote the associated *random edge configuration*. Two extreme site configurations are $\mathbf{1} := \{x_s = 1 : s \in \mathbb{S}_n\} \in \mathbb{X}_n$, with all sites gelled, and $\mathbf{0} := \{x_s = 0 : s \in \mathbb{S}_n\} \in \mathbb{X}_n$, with all sites ungelled. Their corresponding extreme edge configurations are $\mathbf{1} := \{y_{\langle s,r\rangle} = 1 : \langle s,r\rangle \in \mathbb{E}_n\} \in \mathbb{Y}_n$, with all neighboring pairs of sites connected and thus making the material to be in a fully solid state, and $\mathbf{0} := \{y_{\langle s,r\rangle} = 0 : \langle s,r\rangle \in \mathbb{E}_n\} \in \mathbb{Y}_n$, with all neighboring pairs of sites unconnected and thus making the material to be in a fully fluid state, respectively. Note that $Y(x) : \mathbb{X}_n \to \mathbb{Y}_n$ is neither injective nor surjective.

Let $\mathscr{E}(x)$ be the energy of a site configuration x, k be the Boltzmann constant and T be the temperature. Then the probability distribution of interest on the site configuration space $\mathbb{X}_n$ is

$$\pi(x) = \frac{1}{Z_{kT}} \exp\left(-\frac{1}{kT}\mathscr{E}(x)\right) \quad , \quad Z_{kT} = \sum_{x\in\mathbb{X}_n} \exp\left(-\frac{1}{kT}\mathscr{E}(x)\right) \quad ,$$

where Z_{kT} is the normalizing constant or partition function. By $X \sim \pi$, we mean that the random site configuration X has probability distribution π, i.e.,

$$\Pr(X = x) = \begin{cases} \pi(x) & \text{if } x \in \mathbb{X}_n \\ 0 & \text{otherwise} \quad . \end{cases}$$

Next we show that π is a Gibbs distribution by expressing the energy in terms of a potential function describing local interactions. Due to $\{N_s : s \in \mathbb{S}_n\}$, the neighborhood system, we have only singleton and doubleton cliques. Therefore, the Gibbs potential over the two types of cliques are:

$$V_{\{s\}}(x) = (\sigma - \alpha)x_s = \begin{cases} 0 & \text{if } x_s = 0 \\ \sigma - \alpha & \text{if } x_s = 1 \quad , \end{cases}$$

and

$$V_{\langle s,r\rangle}(x) = -\beta x_s x_r = \begin{cases} 0 & \text{if } (x_s, x_r) = (0,0) \\ 0 & \text{if } (x_s, x_r) = (1,0) \\ 0 & \text{if } (x_s, x_r) = (0,1) \\ -\beta & \text{if } (x_s, x_r) = (1,1) \quad , \end{cases}$$

where $\{s\}$ is the singleton clique, $\langle s,r\rangle$ is the doubleton clique with $r \in N_s$, $\sigma \geq 0$ is the external stress applied, $\alpha \geq 0$ is the *site-specific threshold*, and $\beta \in (-\infty, \infty)$ is the *interaction constant* between neighboring sites. The parameters α and β can be thought to reflect fundamental rheological properties of the material under study.

The energy function corresponding to this potential is therefore

$$\begin{aligned} \mathscr{E}(x) &= \sum_C V_C(x) = \sum_{s\in\mathbb{S}_n} V_{\{s\}}(x) + \sum_{\langle s,r\rangle\in\mathbb{E}_n} V_{\langle s,r\rangle}(x) \\ &= \left(-\beta \sum_{\langle s,r\rangle\in\mathbb{E}_n} x_s x_r + (\sigma - \alpha) \sum_{s\in\mathbb{S}_n} x_s\right) \quad . \end{aligned}$$

Since $\mathscr{E}(x)$, the energy of a configuration x, only depends on β and the difference $(\sigma - \alpha)$, we can define this difference as the parameter $\tilde{\sigma} := \sigma - \alpha \geq -\alpha$ in order to reparametrize $\mathscr{E}(x)$ as in (11). Our model satisfies the standard thermodynamic equality as shown in (12).

Let the number of neighbors of site s that are in phase 1 be $x_{N_s} := \sum_{r\in N_s} x_r$. Then, $\mathscr{E}_s(x)$, the *local energy* at site s of configuration x, is obtained by summing the Gibbs potential $V_C(x)$ over all $C \ni s$, i.e., over cliques C containing site s, as derived in (13):

$$\mathscr{E}_s(x) = x_s\left((\sigma - \alpha) - \beta x_{N_s}\right) \quad .$$

Let $(\lambda, x(\mathbb{S}\setminus s))$ denote the configuration that is in phase λ at s and identical to x everywhere else. Then the *local specification* is

$$\pi_s(x) = \frac{\exp(-\frac{1}{kT}\mathscr{E}_s(x))}{\sum_{\lambda\in\Lambda}\exp(-\frac{1}{kT}\mathscr{E}_s(\lambda, x(\mathbb{S}\setminus s)))} = \begin{cases} \frac{\theta}{1+\theta} & \text{if } x_s = 0 \\ \frac{1}{1+\theta} & \text{if } x_s = 1 \end{cases} \quad , \quad (2)$$

where

$$\theta = \theta(s,\alpha,\beta,\sigma) = \exp\left(-\frac{1}{kT}\left(\beta x_{N_s} - (\sigma - \alpha)\right)\right) \quad . \quad (3)$$

In this work we focus on the effect of varying external stress σ at a constant ambient temperature, and therefore without loss of generality, we take $kT = 1$ and work with $\pi(x) = Z_1^{-1}\exp(-\mathscr{E}(x))$.

We can think of our model as an $\mathbb{X}_n$-valued Markov chain $\{X(m)\}_{m=0}^{\infty}$, where $X(m) = (X_s(m), s \in \mathbb{S}_n)$ and $X_s(m) \in \Lambda$, in discrete time $m \in \mathbb{Z}_+ := \{0,1,2,\ldots\}$. Let the initial condition, $X(0) = x(0)$, be given by the initial distribution $\delta_{x(0)}$ over $\mathbb{X}_n$ that is entirely concentrated at state $x(0)$. Then the conditional probability of the Markov chain at time-step m, given that it starts at time 0 in state $x(0)$, is

$$\Pr\{X(m) \,|\, X(0) = x(0)\} = \delta_{x(0)}\left(P_{\alpha,\beta,\sigma}\right)^m \quad , \quad (4)$$

where, the $|\mathbb{X}_n| \times |\mathbb{X}_n|$ transition probability matrix $P_{\alpha,\beta,\sigma}$ over any pair of configurations $(x,x') \in \mathbb{X}_n \times \mathbb{X}_n$ is

$$P_{\alpha,\beta,\sigma}(x,x') = \begin{cases} \frac{1}{n^2}\frac{1}{1+\theta} & \text{if } ||x - x'|| = 1, 0 = x_s \neq x'_s = 1 \\ \frac{1}{n^2}\frac{\theta}{1+\theta} & \text{if } ||x - x'|| = 1, 1 = x_s \neq x'_s = 0 \\ \frac{1}{n^2}\frac{1}{1+\theta} & \text{if } ||x - x'|| = 0, 1 = x_s = x'_s = 1 \\ \frac{1}{n^2}\frac{\theta}{1+\theta} & \text{if } ||x - x'|| = 0, 0 = x_s = x'_s = 0 \\ 0 & \text{otherwise} \quad . \end{cases} \quad (5)$$

and $\theta = \theta(s,\alpha,\beta,\sigma)$, is indeed a function of the site s and the three parameters: α, β and σ. By $||x - x'|| = 1$ we mean that the configurations x and x' differ at exactly site s, i.e., $x_s \neq x'_s$.

Similarly, by $||x-x'||=0$ we mean that the two configurations are identical, i.e., $x=x'$ or $x_s=x'_s$ at every site $s\in\mathbb{S}_n$. We can think of our Markov chain evolving according to the following probabilistic rules based on (2) and (3):

- given the current configuration x, we first choose one of the n^2 sites in $\mathbb{S}_n$ uniformly at random with probability n^{-2},
- denote this chosen site by s and let the number of bondable neighbours of s be $i=x_{N_s}(x)\in\{0,1,2,3,4\}$, and
- finally change the phase at s to 1, i.e., set $x_s=1$ with probability

$$p_i := (1+\theta)^{-1} = (1+\theta(s,\alpha,\beta,\sigma))^{-1} = 1/(1+e^{(\sigma-\alpha-i\beta)}) \tag{6}$$

and set $x_s=0$ with probability $1-p_i$.

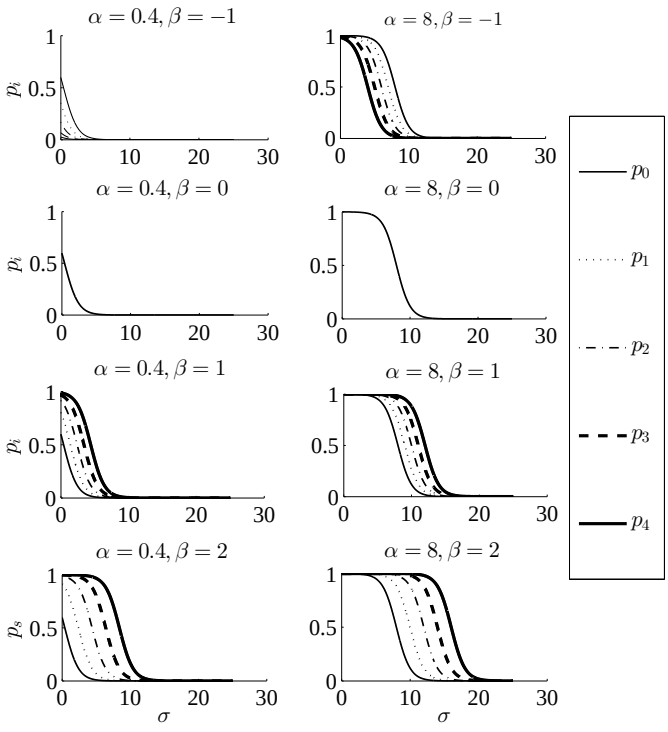

Fig. 5 Plots of p_i, the probability that site s with $i=x_{N_s}$ neighbors in phase 1, is also in phase 1, as a function of external stress σ for different values of α, β. From the plots it is clear that α is a location parameter while β controls the scale of the relative difference between p_i's.

We emphasize the dependence of p_i on the parameters α, β and σ by $p_i(\alpha,\beta,\sigma)$. This is illustrated in Fig. 5 for different parameter values. Just as in the Ising model, our model can be classified into three behavioural regimes depending on the sign of the interaction parameter β. When the interaction parameter $\beta>0$ the model is said to have *agglomerative interactions* analogous to the to the *ferromagnetic* interactions of the Ising model[33] Sec. C.V.4, p.133 whereby the probability of a site being in phase 1 increases with the number of its neighboring sites also being in phase 1, i.e., if $\beta>0$ then

$$0<p_0<p_1<p_2<p_3<p_4<1\ .$$

When $\beta=0$ the model is said to be *non-interactive* since the probability of a site being in phase 1 is independent of the phase of the neighboring sites and identically p at each site, i.e.,

$$0<p=p_0=p_1=p_2=p_3=p_4=1/\left(1+e^{\sigma-\alpha}\right)<1.$$

When $\beta<0$, our model captures the *anti-agglomerative* interactions that are analogous to the *anti-ferromagnetic* interactions of the Ising model[33] Sec. C.V.4, p.133 since the probability of a site being in phase 1 decreases with the number of its neighboring sites also being in phase 1, i.e., if $\beta<0$ then

$$1>p_0>p_1>p_2>p_3>p_4>0\ .$$

Note that our transition probabilities allow *self-transitions*, i.e., there is a positive probability that we will go from a configuration x to itself. Although we think of $\{X(m)\}_{m=0}^{\infty}$ on the state space of all configurations $\mathbb{X}_n$ as a discrete-time Markov chain, with transition probability matrix $P_{\alpha,\beta,\sigma}$ in (5), we can easily add exponentially distributed holding times with rate 1 at each configuration and use (5) to choose a possibly new configuration and thereby obtain a continuous time Markov chain $\{X(t)\}_{t\geq 0}$ in the usual way from $\{X(m)\}_{m=0}^{\infty}$. This Markov chain over $\mathbb{X}_n$ is nothing but our Gibbs field (or Markov random field) model (see for e.g. Ch. 7[34]).

If the external stress varies as a function of discrete time-blocks of length $\underline{h}=\lfloor hn^2\rfloor$ and given by the function $\sigma(m)$ for each time-block $m=0,1,\ldots,M$ then we have the time-inhomogeneous Markov chain $\{X(k)\}_{k=0}^{M\underline{h}}$ with the transition probability matrix at time k given by

$$P(k)=P_{\alpha,\beta,\sigma(\lfloor k/\underline{h}\rfloor)}\ , \tag{7}$$

and the k-step configuration probability, with $k<M\underline{h}$ under initial distribution $\delta_{x(0)}$, given by

$$\Pr\{X(k)=x(k)\,|\,X(0)=x(0)\}$$
$$=\delta_{x(0)}\left(\prod_{m=0}^{\lfloor k/\underline{h}\rfloor}\left(P_{\alpha,\beta,\sigma(m)}\right)^{\underline{h}}\right)\left(P_{\alpha,\beta,\sigma(\lfloor k/\underline{h}\rfloor+1)}\right)^{\overline{(k)}_{\underline{h}}}\ . \tag{8}$$

As before, $\overline{(k)}_{\underline{h}}$ is k modulo $\underline{h}$.

Among the ten models discussed in a detailed review article[33] Sec. C.V. and the classical models of interacting particle systems[36] our Gibbs field model — a parametric family of spin systems or Markov random fields — as described in Appendix B is most closely related to four models: site percolation, voter model, correlated site percolation and a reparametrization of the ising model.

We can use the local specification to obtain the Gibbs sampler, a Monte Carlo Markov chain (MCMC), to simulate from $\{X(m)\}$. Let h denote the average number of hits per site. Thus, $\lfloor h|\mathbb{S}_n|\rfloor=\lfloor hn^2\rfloor$ gives the number of hits on all n^2 sites in $\mathbb{S}_n$ chosen uniformly at random. Given h and the parameters determining the

local specification, i.e., α, β and σ, `GibbsSample`$(x(0),\alpha,\beta,\sigma,h)$ in Algorithm 1 of C produces a sample path of configurations

$$(x(0),x(1),\ldots,x(m)) \in x(0) \times \left(\overset{m}{\underset{i=1}{\times}} \mathbb{X}_n\right) = x(0) \times \mathbb{X}_n^m$$

from the Markov chain $\{X(k)\}_{k=0}^{m}$ given by (4) and (5) and initialized at $x(0)$ as it undergoes $m = \lfloor hn^2 \rfloor$ transitions in $\mathbb{X}_n$.

If we are interested in simulating configurations with stationary distribution $\pi_{\alpha,\beta,\sigma}$, then for large $m = \lfloor hn^2 \rfloor$, the m-step probabilities, $\Pr\{X(m)\,|\,X(0) = x(0)\}$, by construction will approximate samples from $\pi_{\alpha,\beta,\sigma}$ as in (14). We can just as easily produce samples from the time-inhomogeneous Markov chain $\{X(k)\}_{k=0}^{Mh}$ given by (7) and (8) according to Algorithm 2 of Appendix C (see for eg. pp. 21-22[35]).

Two informative singleton clique statistics of a configuration $x(m)$ at time m are the number and fraction of gelled sites given respectively by

$$a(x) := \sum_{s\in\mathbb{S}_n} x_s \quad \text{and} \quad \overline{a}(x) := |\mathbb{S}_n|^{-1} a(x) = \frac{a(x)}{n^2} \ .$$

Similarly, two informative doubleton clique statistics of a configuration x are the number and fraction of connected pairs of neighboring sites given respectively by

$$b(x) := \sum_{\langle s,t\rangle\in\mathbb{E}_n} y_{\langle s,r\rangle} = \sum_{\langle s,r\rangle\in\mathbb{E}_n} x_r x_s \,, \quad \overline{b}(x) := |\mathbb{E}_n|^{-1} b(x) = \frac{b(x)}{2n^2} \ .$$

When the configuration is a function of time m and given by $x(m)$, then the corresponding configuration statistics are also functions of time and are given by: $a(m) = a(x(m))$, $\overline{a}(m) = \overline{a}(x(m))$, $b(m) = b(x(m))$ and $\overline{b}(m) = \overline{b}(x(m))$. The energy of a configuration x can be succinctly expressed in terms of $\overline{a}(x)$ and $\overline{b}(x)$ as

$$\mathscr{E}(x) = -\beta b(x) + (\sigma-\alpha)a(x) = -\beta 2n^2\overline{b}(x) + (\sigma-\alpha)n^2\overline{a}(x) \ ,$$

and therefore

$$\mathscr{E}(x) \propto -2\beta\overline{b}(x) + (\sigma-\alpha)\overline{a}(x) = -2\beta\overline{b}(x) + \tilde{\sigma}\overline{a}(x) \ , \qquad (9)$$

where $\beta \in (-\infty,\infty)$ and $\tilde{\sigma} = \sigma - \alpha \geq -\alpha$ for a given $\alpha \geq 0$. Since the energy of a configuration x, given n, only depends on its $\overline{a}(x)$ and $\overline{b}(x)$, we can easily visualize any sample path $(x(0),\ldots,x(m)) \in \mathbb{X}_n^{m+1}$ in configuration space that is outputted by either Algorithm 1 or Algorithm 2 as the following sequence of $(m+1)$ ordered pairs in the unit square:

$$\left(\left(\overline{a}(x(0)),\overline{b}(x(0))\right),\ldots,\left(\overline{a}(x(m)),\overline{b}(x(m))\right)\right) \in \left([0,1]^2\right)^{m+1} \ .$$

Finally, we reserve upper-case letters for random variables. Thus, $A(X)$, $\overline{A}(X)$, $B(X)$ and $\overline{B}(X)$ are the statistics of the random configuration X. And the notation naturally extends to $A(m)$, $\overline{A}(m)$, $B(m)$ and $\overline{B}(m)$ when $X(m)$ is a random configuration at time m.

The macroscopic behaviour of a configuration x can be described by other statistics of x. We can obtain the connectivity information in the site configuration x through y, its edge configuration, according to (1). By representing the connectivity in y and/or x as the adjacency matrix of the graph whose vertices are $\mathbb{S}_n$, we can obtain various alternative graph statistics:

1. $C_x = \left\{C_x^{(1)}, C_x^{(2)}, \ldots, C_x^{(n_y)}\right\}$, a partition of $\mathbb{S}_n$ that gives the set of connected components of x
2. $C_x^{(*)} = \text{argmax}_{C_x^{(i)}\in C_x} |C_x^{(i)}|$, the first largest connected component
3. $|C_x^{(*)}|/n^2$, the size of the first largest connected component per site
4. $F_x^{(*)}$, the fraction of the rows of $\mathbb{S}_n$ that are permeated (from top to bottom) by $C_x^{(*)}$.

3 Results

In this Section we mainly obtain various insights about the macroscopic behaviour of our model based on Monte Carlo simulations from Algorithms 1 and 2 and make some comparisons with both existing theoretical results and the qualitative yielding behaviour observed in macroscopic experiments. The analysis will be carried on as a function of the applied stress σ, site specific threshold α and the interaction parameter β.

3.1 Behavior under zero stress (stress free gelation, $\sigma = 0$)

In the absence of any external stress, we are interested in the macroscopic behaviour of phase transition from an initial fluid configuration, typically with $x(0) = \mathbf{0}$, to the configuration of a physical gel with a percolation cluster. Recall ~~from Sections 2.5~~ that a percolation cluster (see Appendix B.1) appears when the largest connected component of the configuration x given by $C_x^{(*)}$ spans the entire lattice as indicated by $F_x^{(*)} = 1$. This process is known as *aging* and can be thought of as the process of letting the material rest after having agitated it to a fully fluid state.

Let the initial site configuration be all fluid with $x(0) = \mathbf{0}$ and $(\overline{a}(x(0)),\overline{b}(x(0))) = (0,0)$. We model aging by the time evolution of the site configuration, i.e. by $x(m)$ as $m \to \infty$, or equivalently in rescaled time by $x(t)$ as $t \to \infty$, where $m = \lfloor tn^2 \rfloor$. The material as it ages may or may not form a gel depending on the parameters α and β. For various values of α and β we obtain insights from Monte Carlo simulations of stress-free gelation, i.e., for the fluid-solid (F-S) phase transition to occur in the absence of external stress.

Site percolation model of Sec. B.1 with *site-filling probability* p, which gives the probability of a site being in phase 1, has been used (see[26,33] and references therein) to model gelation over time. In these studies percolation transition as p varies is used to model gel transition. In our approach we treat α, the site-specific threshold, and β, the interaction constant, as fixed rheological parameters that characterize the nature of the given yield stress material. Recall that α and β specify the Gibbs potential over the two types of cliques in order to give the energy of a site configuration under a given external stress σ (as derived in Sec. 2). When we study the possible gelation of a material with a given α and β we do not think of varying the site-filling probability directly, as in[26], but rather let it be defined by α and β in a possibly

configuration-dependent manner. Thus, if we find that gelation occurs for a specific value of (α,β), say $(8,1)$, then we interpret this as the gelation of the material with $(\alpha,\beta)=(8,1)$ in the absence of external stress, i.e. the material evolves probabilistically on the configuration space from the completely fluid configuration of $\mathbf{0}$ to one with a percolation cluster. Thus our approach to modeling gelation is not only microscopic but also mechanistic, in terms of allowing the nature of stochastic evolution in the configuration space to depend on the fixed rheological parameters α and β.

Recall that our non-interactive model with $\beta=0$, in the absence of any external stress ($\sigma=0$), is the site percolation model with site-filling probability $p=(1+e^{-\alpha})^{-1}$. When $\beta=0$ and $p=(1+e^{-\alpha})^{-1}\geq p_c\approxeq 0.5927$, the critical site percolation probability, we have a large *percolation cluster* of gelled sites that permeates through out the material and turns the material into a gel. If $(1+e^{-\alpha})^{-1}<p_c$ then the material, as it ages, will not form a percolation cluster and therefore remain as a fluid. The critical value p_c of the site-filling probability p can be transformed into a critical value α_c of the rheological parameter α, in the absence of interaction ($\beta=0$) and external stress ($\sigma=0$) as follows:

$$\alpha\geq\alpha_c=-\ln(p_c^{-1}-1)=-\ln(0.5927^{-1}-1)\approxeq 0.37513\ . \quad (10)$$

Thus, if $\beta=0$, $\sigma=0$ and the rheological parameter $\alpha\geq\alpha_c$ then the material will cross the *bulk gel point* and turn into a solid on the basis of the classical site percolation model. On the other hand, if $\beta=0$, $\sigma=0$ and $\alpha<\alpha_c$ then it will remain as a fluid.

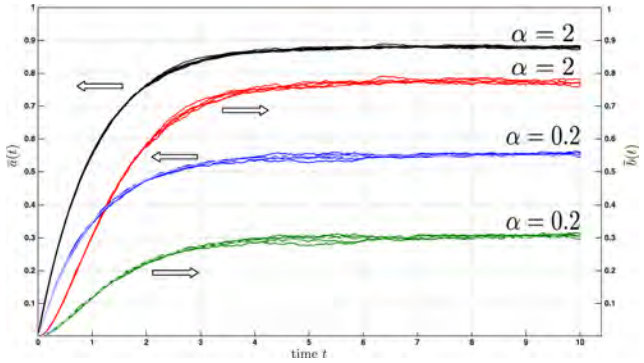

Fig. 6 Plots of five simulated realizations $\overline{a}(t)$ (left vertical axis, see the left pointing arrows) and $\overline{b}(t)$ (right vertical axis, see the right pointing arrows) of the configuration statistics $\overline{A}(t)$ and $\overline{B}(t)$ as a function of rescaled simulation time t (in units of $n^2=10^4$) when the external stress is $\sigma=0$, initial condition $\mathbf{0}$, $\beta=0$ and two values for $\alpha\in\{0.2,2.0\}$.

Figure 6 illustrates five realizations of $\overline{A}(t)$ and $\overline{B}(t)$ from the Gibbs Sampler for the initial condition $\overline{a}(0)=0$ based on the site configuration being initialized at the all-zero state $x(0)=\mathbf{0}$ in the absence of any external stress, $\sigma=0$.

The realisations of $\overline{a}(t)$ when $\alpha=0.2<\alpha_c$ and $\beta=0$ indicate no gel is being formed, i.e. $\Pr\{F_X^{(*)}=1\}=0$, because the site-filling probability $p=1+e^{-0.2}=0.549834$ is below the critical site percolation probability $p_c\approxeq 0.5927$. On the other hand, the realisations of $\overline{a}(t)$ when $\alpha=2\geq\alpha_c$ are consistent with a gel being formed, i.e. $\Pr\{F_X^{(*)}=1\}>0$, since the site-filling probability $p=1+e^{-2}\approxeq 0.8808$ is greater than p_c.

If $\beta>0$ then our model, being a particular parametric family of correlated site percolation, allows for the site-filling probability p_i at site s to be site-specific by making it depend on $i=x_{N_s}$, the number of neighboring sites of s that are in phase 1. Thus, the site-filling probability changes site-specifically with the configuration $x(m)$ at time m. If $\beta\geq 0$ and $\alpha>\alpha_c$ then p_i, the site-filling probability at every site s, in the absence of any external stress ($\sigma=0$), is at least as high as the critical percolation probability p_c. This is sufficient for the formation of the percolation cluster and attain stress-free gelation. Recall that p_c for site percolation is not known analytically but estimated consistently from Monte Carlo simulations even when $\beta=0$. We can similarly obtain Monte Carlo estimates of a bi-partition of a large subset of the parameter space, say $\{(\alpha,\beta):\alpha\in[10^{-4},10]\times[10^{-4},10]\}$, into a *gellable* subset of parameters that lead to the formation of a gel and another *ungellable* subset of parameters that do not, using Algorithm 1.

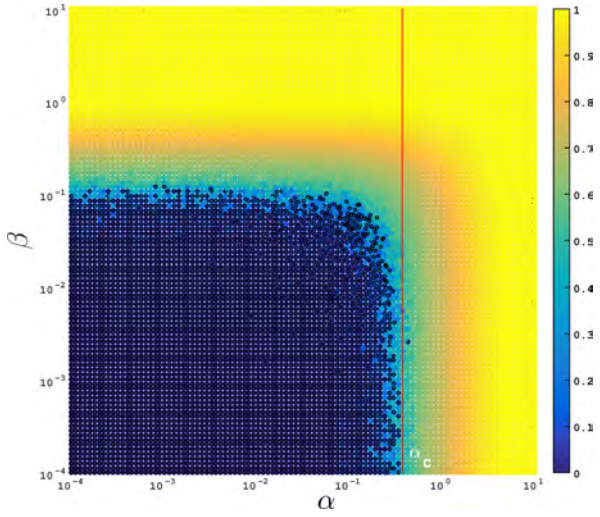

Fig. 7 The shading of the circle at each (α,β) indicates $F_{x(100)}^{(*)}$, the proportion of the lattice occupied by the largest cluster of gelled sites at rescaled time $t=100$ after having initialized from the all fluid configuration $\mathbf{0}$ in the absence of external stress. Parameter values that do not lead to a percolation cluster after each one of the $n^2=10^4$ sites has undergone 100 transitions (on average), i.e. with $F_{x(100)}^{(*)}<1$, are highlighted by circles with black boundary.

For a given parameter value (α,β) in a set made from the union of logarithmically, linearly and quasi-randomly spaced points in $[10^{-4},10]^2$ we can simulate site configurations $x(m)$ according to Algorithm 1 with $\sigma=0$ and initial fluid configuration $x(0)=\mathbf{0}$ as m approaches a large number, say 10^6. Figure 7 shows, over a grid of parameters in $[10^{-4},10]^2$, the nearly asymptotic value of $F_{x(100)}^{(*)}$, the proportion of the lattice with $n^2=10^4$ sites that is occupied by the largest cluster (connected component) of gelled sites at a large discrete time $m=10^6$ or rescaled time $t=100$ after each site has undergone $h=100$ transitions on average. The set of *ungellable* parameters are estimated to be those whose $F_{x(100)}^{(*)}<1$ and are highlighted by circles with black boundaries in the lower left corner of Fig. 7. The set of parameters with $F_{x(100)}^{(*)}=1$ are

estimated to be *gellable* and depicted in Fig. 7 by shaded circles without a black boundary. These estimates are only based on one simulation per (α,β) and just meant to give a rough idea of gel formation. However, the characteristics of the bi-partition of the parameter space into gellable and ungellable regions are similar to Figure 7 when we increased the lattice size n from 100^2 to 200^2 and the duration t from 100 to 200 (results not shown). By doing multiple independent simulations per parameter value over a larger lattice ($n > 10^4$) and longer time ($t > 100$) one can easily obtain asymptotically consistent estimates (with standard errors) for the (α,β)-specific probability that $F^{(*)}_{x(t)} = 1$ as $t \to \infty$ and $n \to \infty$ using Algorithm 1.

From Figure 7 it is clear that the material gets gelled in the absence of external stress not only when $\alpha > \alpha_c \approxeq 0.37513$ (the vertical line in Fig. 7 goes through α_c) but also for smaller values of α, provided β is large enough to compensate and increase the site-filling probability. In the sequel, we are mainly interested in values of α much larger than α_c, say $\alpha = 8$ without loss of generality, in order to focus on yield stress materials that can form a gel with a high probability under zero stress. This concludes our study of *stress-free gelation*, i.e. the possibility of a fluid to solid phase transition under zero external stress.

3.2 Equilibrium behaviour under constant stress

We are interested in the effect of applying constant external stress σ for a long period of time to an yield stress material with rheological properties specified by parameters α and β.

The sub-plot **(a)** of Fig. 8 approximates the time asymptotic behaviour of $\bar{a}$ when the Monte Carlo simulation of Gibbs field was initialized from **1** (using Algorithm 1 with $h = 100$) and sub-plot **(b)** presents the same information when the Gibbs field was initialized from **0**. For both simulations we have used $n = 100$ and $(\tilde{\sigma},\beta)$ taken from a grid of linearly spaced points in $[-10,15]\times[0,4]$. In both panels (a-b) of Fig. 8 one can note that if the interaction parameter is smaller than a critical value of the interaction parameter $\beta < \beta_c$ ($\beta_c \approx 1.5$), both the solid-fluid and fluid-solid transitions are smooth. When the interaction parameter β is gradually increased past this critical value both transitions become increasingly sharp.

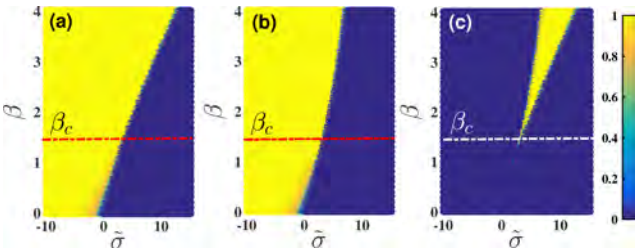

Fig. 8 The value of $\bar{a}$ at rescaled time $t = 100$ from Monte Carlo simulations of the Gibbs field using Algorithm 1 for fixed parameters $(\tilde{\sigma},\beta)$ when initialized from **1** (panel **(a)**) and from **0** (panel **(b)**). The difference in $\bar{a}$ between the sub-plots **(a)** and **(b)** is shown in panel **(c)**. The horizontal dashed lines indicate the critical value of the interacting parameter β_c (see the discussion in the text).

To assess the reversibility of the deformation states in the time asymptotic limit we focus at the difference between the sub-plots (a) and (b) which is presented in Fig. 8(c). In the range $\beta < \beta_c$ the steady state transition from solid to fluid evolves through the same intermediate states as the steady state transition from fluid to solid and no hysteresis effect can be observed. When the interaction parameter β exceeds the critical value β_c a triangular hysteresis region may be observed in Fig. 8(c).

This is an interesting result as it tells us that in the presence of strong interactions a "*genuine*" hysteresis of the deformation states would be observed even in conditions of a steady state forcing. At a given applied stress $\tilde{\sigma}$ the size of the hysteresis region increases when the strength of the interactions is increased.

3.3 Configurations at the Solid-Fluid Interface

We are now interested in the nature of the configuration x for a given β at the solid-fluid interface, i.e. when $\bar{a} = 1/2$, as $\tilde{\sigma}$ reaches a specific value. Site configurations at the solid-fluid interface provide the random environment for restricted diffusion of small tracer particles near gel transition. This phenomenon is of experimental and theoretical interest[13,27,28] and has been recently studied for the case of $\beta = 0$[26]. We are interested here in gaining insights on the nature of the site configurations at the solid-fluid interface for values of β below, above and equal to zero.

Figure 9 shows two random site configurations at the solid-fluid interface when $\bar{a} \approxeq 1/2$ for three different values of β. Without loss of generality, we fixed $\alpha = 8$, and focus on the properties of the material that is capable of forming a gel in the absence of external stress. Clearly, the site configurations are dependent on the magnitude and sign of the interaction parameter β. Recall that $\bar{a}$, the fraction of gelled sites, and $\bar{b}$, the fraction of pairs of neighboring gelled sites, are the sufficient statistic of the configuration, i.e. the energy of the configuration only depends on its $(\bar{a},\bar{b})$.

3.3.1 Configurations when $\bar{a} \approxeq 1/2$ and $\beta = 0$

If $\beta = 0$, the non-interactive case of the classical site percolation model studied in[26], and $\tilde{\sigma}$ is chosen so that $\bar{a} = 1/2$ then due to the site-filling probability being independently and identically distributed across all n^2 sites $\bar{b} = \bar{a}^2 = 1/4$. Two typical configurations when $\beta = 0$, $n = 100$ and $t = 100$ at the solid-fluid interface are shown by the sub-plots in the second row of Fig. 9. More configurations were visually explored and their distinguishing site configuration feature is characterized by the independence of the site-filling probability over sites and is apparent by the concentration of their sufficient statistics $(\bar{a},\bar{b})$ about $(\bar{a},\bar{a}^2) = (1/2,1/4)$ at the solid-fluid interface. This is the only case considered by[26] when obtaining the random environment for restricted diffusion of small tracer particles near gel transition.

3.3.2 Configurations when $\bar{a} \approxeq 1/2$ and $\beta = 2$

When we increase β from 0 to 2 we have a very different distribution over site configurations at the solid-fluid interface as shown by two samples in the first (top) row of Fig. 9. It is easy to understand this "patchy" pattern in site configurations with large positive β by realizing that new gelled sites can occur with a higher probability at sites neighboring existing gelled sites that have a larger $i = x_{N_s}$, number of neighbors in phase 1, than at sites sur-

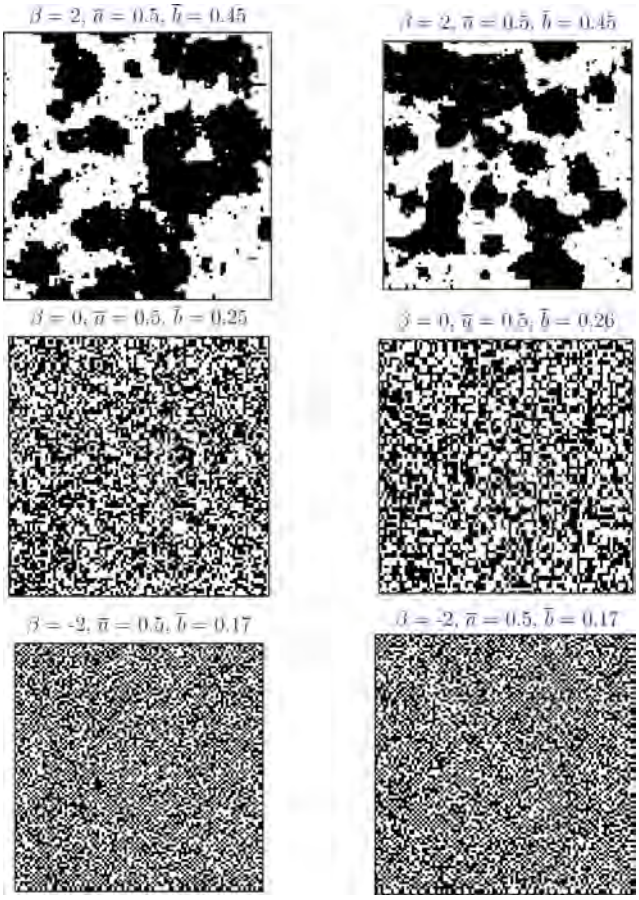

Fig. 9 Effect of β on preferred energy minimizing configurations. Two sample configurations are shown for each $\beta \in \{-2, 0, +2\}$ over a toroidal square lattice of 100×100 sites. Sites in phase 0 and 1 are shown in black and white, respectively, at the solid-fluid interface when $\overline{a} \approxeq 1/2$.

rounded by ungelled sites with a smaller $i = x_{N_s}$ (see bottom two rows of Fig. 5). As β gets larger, the probability of forming gelled sites around existing gelled sites is much larger than that of forming gelled sites around ungelled sites, and this concentrates $(\overline{a}, \overline{b})$ about $(\overline{a}, \overline{a}) = (1/2, 1/2)$ at the solid-fluid interface.

3.3.3 Configurations when $\overline{a} \approxeq 1/2$ and $\beta = -2$

Finally, when we decrease β from 0 to -2 we have a "checkered" pattern of site configurations at the solid-fluid interface as shown by two samples in the third (bottom) row of Fig. 9. As β gets negative, the probability of forming gelled sites around existing gelled sites gets much smaller (see top row of Fig. 5). In the extreme asymptotic case, as $\beta \to -\infty$, we obtain configurations with increasingly checkered patters with $(\overline{a}, \overline{b}) \to (1/2, 0)$, the sufficient statistics of the extreme "chess board" configuration (such patterns occur already for $\beta = -8$ with $n = 100$ but are not shown here).

Thus, from the β-dependent site configurations at the solid-fluid interface depicted in Fig. 9, it is clear that the trajectories of tracer particles (see Fig. 1 of[13] from[27]) that can only diffuse through the ungelled (black) contiguous regions are heavily dependent on whether there is interaction between adjacent gelled sites. This interaction is captured in our correlated site percolation model by the interaction parameter β.

3.4 Behavior under varying stress

The energy of $X(t)$, the random site configuration at time t, depends on two of its highly correlated statistics: $\overline{A}(t)$, the random fraction of gelled sites at time t, and $\overline{B}(t)$, the random fraction of connected sites at time t. One of our primary interests is to study $\overline{A}(t)$ and $\overline{B}(t)$ as $X(t)$ is under the influence of time-varying externally applied stress $\sigma(t)$.

Using Monte Carlo simulations from Algorithm 2 of the time-inhomogeneous Markov chain $\{X(m)\}_{m=0}^{Mh}$ given by (7) and (8), under an initially increasing and subsequently decreasing time-dependent stress $\sigma(m)$ given in the bottom panel of Figure 10, we obtained multiple independent trajectories of $\overline{A}(\sigma)$, the fraction of gelled sites as a function of the external stress σ. Five such simulated trajectories are shown in the first four panels of Figure 10. In order to mimic an asymptotic steady state of deformation (which is typically what a rheologist would be interested in characterising during a rheological measurement) the holding time per stress value has been chosen large, $h = 1000$ hits per site. We note that regardless the value of the interaction parameter β the results of the five individual simulations overlap nearly perfectly which indicates that the grid size of the simulation is sufficiently large and the simulated trajectories are robust.

For low values of the interaction parameter ($\beta \in \{0, 1\}$, top row of Figure 10) the dependence $\overline{a}(\sigma)$ corresponding to the decreasing branch of the stress ramp overlaps with that corresponding to the increasing branch and no hysteresis is observed. This indicates that in the presence of weak interactions and provided that an asymptotically steady state is reached the deformation states are fully reversible upon increasing/decreasing the external forces. In this case a smooth solid-fluid transition is observed.

As the value of the interaction parameter is increased ($\beta \in$

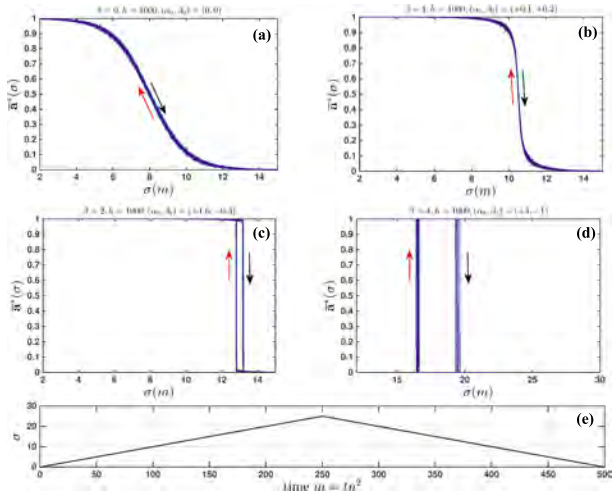

Fig. 10 Results of five distinct Gibbs field simulations corresponding to an increasing/decreasing stress ramp (illustrated in the bottom panel) with $\alpha = 8$ and $\beta \in \{0,1,2,4\}$ indicated on the top of each panel). The stress was increased from 0 to 25 in units of 0.01 and decreased back to 0 with a holding time of $h = 1000$ (nearly asymptotic state for each value of the applied stress) as the site configuration varied from **1** to **0** and then back to **1**. The arrows indicate the increasing/decreasing branches of the stress ramp.

$\{2,4\}$, middle row of Figure 10) a significantly different yielding behaviour is observed. First, the deformation states are no longer reproducible upon increasing/decreasing stresses and a clear hysteresis is observed. Second, larger the value of the interaction parameter is, steeper the solid-fluid transition becomes.

To conclude this part, the realizations of the time-inhomogeneous Markov chain under time-dependent stress $\sigma(m)$ corresponding to an asymptotically steady forcing reveal a smooth and reversible solid-fluid transition if the interactions are either absent or weak and a steep and irreversible transition in the presence of strong interactions. This result is consistent with the result presented in Fig. 8 where we have seen that for $\beta > \beta_c$ a genuine irreversibility of the deformation state is observed during the steady yielding process. An experimental validation of these conclusions has been recently presented[5]. The rheological flow curves measured for a suspension of spherical and electrically charged non-motile micro algae (*Chlorella Vulgaris*) reveal an abrupt solid-fluid transition and exhibit a strong hysteresis even in the limit of very slow forcing, see Fig. 11 in[5]. In the case of a Carbopol gel where the microscopic interactions are presumably weaker than the interactions between electrically charged Chlorella cell a much smoother solid fluid transition is observed and, in the asymptotic limit of steady forcing, the hysteresis effects become negligibly small,[13]. This is perhaps the main reason why Carbopol gels have been considered for decades "*model*", "*simple*" or "*ideal*" yield stress fluids.

3.4.1 Effect of holding time (steadiness of the external forcing) on the hysteresis

A large number of flows of yield stress fluids are unsteady in the sense that the applied stress is maintained for a finite time t_0. For the case of a rheometric configuration, we have illustrated the unsteady response of the material in Fig. 2. An important feature of the deformation curves presented in Fig. 2 is the irreversibility of the deformation states upon increasing/decreasing applied stresses. The magnitude of this effect is found to depend systematically on the degree of steadiness of the forcing, the time t_0 the applied stress is maintained constant, Fig. 3.

The question we address in the following is to what extend is our Gibbs field model able to describe the unsteady yielding behaviour observed in macroscopic experiments. To answer this question we calculate trajectories $\bar{a}$ similar to those presented in Fig. 10 which are realised during an increasing/decreasing stress ramp (see the bottom panel of Fig. 10).

To place ourselves in the conditions of an unsteady forcing, we chose during the simulations finite values of the holding time (or average number of hits per site). We note that the average holding time per site in our simulations is the closest equivalent we could find for the characteristic forcing time t_0 imposed during macroscopic rheological measurements, see Figs. 2, 3 and the discussion in Sec.1. To quantify the degree of reversibility of the deformation states, we calculate after each run the area of the hysteresis encompassed by the increasing/decreasing branches of the dependence $\bar{a} = \bar{a}(\sigma)$.

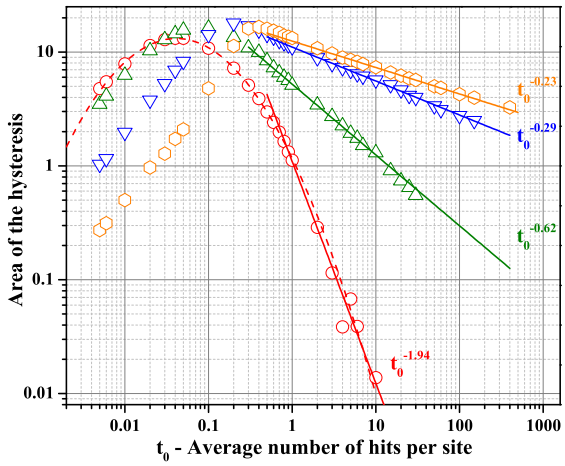

Fig. 11 Effect of increasing β on the relative hysteresis area for $\bar{a}$ for different holding times t_0 per stress level in a stress ramp from 0 to 25 in increments of 1 (with $\alpha = 8$). The dash line is a log-normal fit and the full lines are the fitted power laws indicated in the inserts. The symbols refer to the value of the interaction parameter β: circles (○) - $\beta = 0$, up triangles (△) - $\beta = 1.5$, down triangles (▽) - $\beta = 3$, hexagons (⬡) - $\beta = 3.5$.

The dependencies of the hysteresis area on the holding time obtained from such simulations performed for a fixed value of the site threshold α and several values of the interaction parameter β are presented in Fig.11.

Regardless the strength β of the interaction, a non monotone dependence of the hysteresis area on the holding time is obtained. By carefully inspecting the individual dependencies $\bar{a} = \bar{a}(\sigma)$, we have noticed that prior to the local maximum the lattice yields only partially ($\bar{a}$ never reaches 0) corresponding to the largest value of the applied stress σ. Corresponding to the local maxima $t_0^\star$ of the dependencies presented in 11 the lattice yields com-

pletely (the terminal value of $\bar{a}$ is 0) and the area of the hysteresis starts decaying with the holding time t_0. This behaviour of the degree of irreversibility of deformation states as a function of the steadiness of the forcing is qualitatively similar to the experimental results illustrated in Fig. 3. In the absence of interactions ($\beta = 0$), the hysteresis area follows a log-normal correlation with the holding time (see the circles and the dashed line in Fig. 11) which once more comes into a qualitative agreement with the experimental results. For non zero values of β we could not accurately fit the data by a log-normal function. Corresponding to the largest values of the average number of hits per site we have tested, we have found a power law decay of the hysteresis area, the full lines Fig. 11) which is once again similar to the behaviour illustrated in Fig. 3 and consistent with experimental results obtained with Carbopol gels,[13,15].

It is equally interesting to note that stronger the interaction is (larger the parameter β is), weaker the decay of the hysteresis area with the characteristic forcing time t_0 is. This indicates that in the presence of strong interactions a full reversibility of the deformation states can not be achieved regardless the degree of steadiness of the external forcing. This is indeed the case of several highly thixotropic materials such as bentonite gels, laponite gels where steady state rheological measurements can not be truly achieved even during very slow controlled stress flow ramps. Among the data we illustrate in Figs. 2, 3, the mayonnaise seems to behave as such as well.

4 Discussion

In summary, using a site-specific threshold α and an interaction constant β as two fixed parameters for a given material, and an externally applied stress σ, we derive a thermodynamically consistent correlated site percolation model over a toroidal square lattice. This Markov chain over the space of site configurations can be simulated using Gibbs sampling schemes given by Algorithms 1 and 2. The simulations from Algorithms 1 and 2 were used to gain several macroscopic insights about the solid fluid transition in yield stress fluids and were found to be in qualitative and quantitative agreement with known empirical results. For example, our model accounts for the effect of non-zero β on preferred site configurations at the solid-fluid interface when $\bar{a} = 1/2$ as shown in Fig. 9. The β-dependent micro-structure of the interface at this bulk gel point clearly influences the motion of the micro-sized tracer particles as studied by[26] (but only for the non-interactive case with $\beta = 0$). For example it is clear from the configurations close to the gel point that a large negative β creates a chess-board pattern of gelled and ungelled sites that would prohibit the motion of tracers from their most recent positions while a large positive β with agglomerative clumping of gelled sites allows more navigable room for the tracers. de Bruyn[26] concludes that their simulations (with $\beta = 0$) do not reproduce the scaling behaviour displayed by the microrheological moduli in experiments on materials near their gel point. Although we do not pursue the properties of tracer particle motion at the gel point in this work we expect it to be an interesting future pursuit using non-zero values of β.

Our model provides several interesting insights into the yielding transition. In the limit of an asymptotically steady forcing (a constant stress is maintained over very long times), the steepness of the solid-fluid transition is solely controlled by the magnitude of the interactions, β. In the absence of interactions or in the presence of weak interactions, the solid-fluid transition is smooth and the deformation states are reversible upon increasing/decreasing stresses, see panels (a, b) in Fig.10. If the interaction parameter is increased past a critical value $\beta_c \approx 1.5$, the solid-fluid transition becomes increasingly steeper and irreversible upon increasing and decreasing stresses, see panels (c, d) in Fig.10. Qualitatively, this results is in good agreement with the rheological measurements performed on highly thixotropic materials (see for example panel (a) in Fig. 2) which reveal a rheological hysteresis even in the conditions of a steady state forcing.

For the case of an unsteady forcing (i.e. the stress is applied during a finite time t_0) our model predicts that the deformation states are generally not recoverable upon increasing/decreasing stresses past the solid-fluid transition and a hysteresis of the deformation states will be observed even in the absence of interactions. This comes into a good agreement with the unsteady rheological measurements performed with aqueous solutions of Carbopol at various concentrations and operating temperature, see panel (c) in Fig. 2 and Refs.[13–15]. We find that, regardless the strength β of the interactions, the magnitude of the hysteresis depends non monotonically on the degree of steadiness of the forcing t_0, Fig. 11 which once more agrees qualitatively with the experimental observations illustrated in Fig. 3.

In closing, in spite of a very limited number of parameters involved (namely α and β), the Gibbs field model presented through our manuscript is able to capture the main qualitative features of the solid-fluid transition of a yield stress material subjected to either steadily or unsteadily varying external stresses. Bearing in mind that we did not assign any particular constitutive relation to the solid and fluid phases and we did not account for the motion of solid and fluid elements during the transition (there exists no equivalent of the shear rate $\dot{\gamma}$ in our model) one may suggest that the main qualitative features of the yielding process we have highlighted in Sec. 1 originate from the stochastic nature of the destruction and re-formation of solid structural units and not from the rheological properties of the phases. In this regard our model is quite universal and might be used to describe the yielding of a broad class of molecularly different materials. Last, there are several interesting directions to pursue in future studies.

First, a more detailed model that simultaneously represents the fraction of gelled sites and the fraction of bonds in one dependent system would provide a better quantitative and qualitative approximation of the correlated site percolation model. Second, an alternative interesting extension of our model could involve allowing for solvent effects through a model akin to *correlated site-bond percolation* of[33] Sec. D.II., p.136 but with our focus on external stress as opposed to temperature. In such a model we have an additional parameter that allows for a site to be occupied by a monomer with probability ϕ and by the solvent with probability $1-\phi$. Third, we believe it would be interesting to extend the micro-rheological study first initiated by de Bruyn[26] by considering lattices generated from the Gibbs algorithm we have

presented during various stages of the solid-fluid transition.

Acknowledgements

This collaborative work commenced during TB's visit to University of Canterbury (UC) in 2012 with partial support from a research grant to MM-G from UC's College of Engineering and by the project ThIM (project ANR10 BLAN 0925-01) from the National French Research Agency (ANR). TB is grateful to Dr. Cathy Castelain for numerous discussions on the solid-fluid transition. RS and MM-G visited Nantes in 2013 with partial support from the project ThIM, the Laboratoire de Thermocinétique de Nantes (LTN UMR 6607) and research travel grants from UC's College of Engineering. RS was partly supported in 2014 by a visiting scholarship at Department of Mathematics, Cornell University, Ithaca, NY, USA, a sabbatical grant from College of Engineering, University of Canterbury, and consulting revenues from Wynyard Group, Christchurch, NZ. We thank two anonymous reviewers for improving the presentation of the paper.

A Modelling Details

Since $\mathscr{E}(x)$, the energy of a configuration x, only depends on β and the difference $(\sigma-\alpha)$, we can define this difference as the parameter $\tilde{\sigma} := \sigma - \alpha \geq -\alpha$ in order to reparametrize $\mathscr{E}(x)$ as

$$\mathscr{E}(x) = \left(-\beta \sum_{\langle s,r\rangle \in \mathbb{E}_n} x_s x_r + \tilde{\sigma} \sum_{s\in\mathbb{S}_n} x_s \right) \ , \tag{11}$$

through $(\tilde{\sigma},\beta) \in [-\alpha,\infty)\times(-\infty,\infty)$.

Let the expectation of a function $g : \mathbb{X}_n \to \mathbb{R}$, with respect to π, be

$$\mathbf{E}_\pi(g) := \sum_{x\in\mathbb{X}_n} g(x)\pi(x)$$

then the *internal energy* of the system is

$$\mathscr{U} = \mathbf{E}_\pi(\mathscr{E}) = \sum_{x\in\mathbb{X}_n} \mathscr{E}(x)\pi(x) \ ,$$

and the *free energy* of the system is

$$\mathscr{F} = -kT\ln(Z_{kT}) \ .$$

Our model satisfies the standard thermodynamic equality:

$$\begin{aligned} -T^2\frac{\partial}{\partial T}\left(\frac{\mathscr{F}}{T}\right) &= -T^2\frac{\partial}{\partial T}\left(\frac{-kT\ln(Z_{kT})}{T}\right) = kT^2\frac{\partial}{\partial T}\left(\ln(Z_{kT})\right) \\ &= kT^2\frac{1}{Z_{kT}}\frac{\partial}{\partial T}(Z_{kT}) = kT^2\frac{1}{Z_{kT}}\frac{\partial}{\partial T}\left(\sum_{x\in\mathbb{X}_n}\exp\left(-\frac{1}{kT}\mathscr{E}(x)\right)\right) \\ &= kT^2\frac{1}{Z_{kT}}\left(\sum_{x\in\mathbb{X}_n}\exp\left(-\frac{1}{kT}\mathscr{E}(x)\right)\frac{\mathscr{E}(x)}{kT^2}\right) = \sum_{x\in\mathbb{X}_n}\mathscr{E}(x)\pi(x) \\ &= \mathscr{U} \ . \end{aligned} \tag{12}$$

We sometimes emphasize the dependence of the energy and the corresponding distribution upon α, β and σ by subscripting as follows:

$$\mathscr{E}(x) = \mathscr{E}_{\alpha,\beta,\sigma}(x) \quad \text{and} \quad \pi(x) = \pi_{\alpha,\beta,\sigma}(x) \ .$$

The local energy at site s is derived as follows:

$$\begin{aligned} \mathscr{E}_s(x) &= \sum_{C\ni s} V_C(x) = V_{\{s\}}(x) + \sum_{r\in N_s} V_{\langle s,r\rangle}(x) \\ &= (\sigma-\alpha)x_s - \beta\sum_{r\in N_s} x_s x_r \\ &= x_s\left((\sigma-\alpha) - \beta\sum_{r\in N_s} x_r\right) \\ &= x_s\left((\sigma-\alpha) - \beta x_{N_s}\right) \ . \end{aligned} \tag{13}$$

For large $m = \lfloor hn^2 \rfloor$, the m-step probabilities, $\Pr\{X(m)\,|\,X(0)=x(0)\}$ will approximate samples from $\pi_{\alpha,\beta,\sigma}$:

$$\lim_{m\to\infty} d_{TV}\left(\Pr\{X(m)\,|\,X(0)=x(0)\}, \pi_{\alpha,\beta,\sigma}\right) = 0 \ . \tag{14}$$

Here, $d_{TV}(\varpi,\pi) = 2^{-1}\sum_{x\in\mathbb{X}_n}|\varpi(x)-\pi(x)|$ is the total variation distance between two distributions ϖ and π over $\mathbb{X}_n$ (see for e.g. Ch. 7, Sec. 6[34]).

B Relations to Existing Models

B.1 Site Percolation Model

In a site percolation model, a randomly chosen fraction p of sites are set to be in phase 1; these sites represent gelled regions of the material while the remaining sites in phase 0 represent ungelled or fluid regions. In our approach we treat α, the site-specific threshold, and β, the interaction constant, as fixed parameters that characterize the nature of the given yield stress material. When we study the possible gelation of a material with a given α and β we do not think of varying the site-filling probability directly, as in[26], but rather let it be defined by α and β in a possibly configuration-dependent manner. Thus our approach to modeling gelation is not only microscopic but also mechanistic, in terms of allowing the nature of stochastic evolution in the configuration space to depend on the fixed rheological parameters α and β. Our non-interactive model ($\beta = 0$) in the presence of a constant external stress ($\sigma \in [0,\infty)$) is the site percolation model over $\mathbb{S}_n$ with site-filling probability $p = (1+e^{\sigma-\alpha})^{-1}$. In the absence of external stress with $\sigma = 0$ we have the site percolation model with site-filling probability $p = (1+e^{-\alpha})^{-1}$. As p increases from 0, the size of the largest connected region of gelled sites grows and at a critical probability $p = p_c \approxeq 0.5927$ (for large n) a *percolation cluster* that spans the entire lattice $\mathbb{S}_n$ appears when $F_x^{(*)} = 1$ for site configuration x. We note that the value of p_c for site percolation, unlike for bond percolation where we only track the presence or absence of bonds between adjacent sites, is not yet known exactly (although various inequalities, identities and asymptotically consistent point estimates are known[37] for e.g. see Secs. 5.3,6.1,6.4). Finally, site percolation is more general than bond percolation and can, at least in principle, be used to model richer phenomena. Our interpretation of the site configuration where each site is either bondable or unbondable and its associated edge configuration where only two neighboring bondable sites form a bond, is not as strict as the interpretation in the *random-site percolation* model of[33] Sec. C.V.1, p.130 that "bonds between sites always

exist". In our interpretation, bonds between sites only exist if two neighboring sites are bondable, i.e., they are both in phase 1.

B.2 Voter Model

Our model is closely related to the embedded discrete time Markov chain in the classical *voter process*[36] Ch. 5 of probability theory, whereby at each site a voter casts one of two votes (0 or 1) by copying the vote of one of its randomly chosen four nearest neighbors in $\mathbb{S}_n$. If the voter at each site chooses one of its four neighbors uniformly at random, then the voter model corresponds to our model with

$$p_0 = 0, p_1 = 1/4, p_2 = 1/2, p_3 = 3/4, p_4 = 1 \ . \tag{15}$$

More generally, one can allow $0 \le p_0 \le p_1 \le p_2 \le p_3 \le p_4 \le 1$ to recover a corresponding voter process that is possibly influenced by the neighboring votes. Thus, in the square lattice $\mathbb{S}_n$ with four nearest neighbors, every point $(p_0, p_1, \ldots, p_4)$ in $\triangle^4$, the unit 4-simplex containing the set of all probability mass functions over $\{0,1,2,3,4\}$, defines a voter process. We can think of $\triangle^4$-indexed voter process as a discrete non-parametric extension of the classical parameter-free voter process of (15).

Finally, for a fixed $\beta \in (-\infty, \infty)$ and a fixed $\tilde{\sigma} = \sigma - \alpha \ge -\alpha$, our model can be thought of as a $(\tilde{\sigma}, \beta)$-parametric specification of the discrete time voter model (which can be extended in the usual way to continuous time by introducing independent exponential holding times with rate 1). For example, with $kT = 1$, $\beta = \ln(3)$ and $\tilde{\sigma} = \sigma - \alpha = 2\ln(3)$, we can get the parameters of our model to be close to that of the classical voter model in (15) but with

$$p_0 = 1/10, p_1 = 1/4, p_2 = 1/2, p_3 = 3/4, p_4 = 9/10 \ .$$

We note that the classical voter model allows for extreme probabilities with $p_0 = 0$ and $p_1 = 1$ and this turns the two extreme site configurations with all 0's and all 1's, i.e., **0** and **1**, into absorbing states. However, in our model the probabilities are non-extreme, i.e., $0 < p_0 < 1$ and $0 < p_1 < 1$, and thus our Markov chain is irreducible and aperiodic (due to self-transitions) on the large but finite configuration space $\mathbb{X}_n$. Moreover, when $\beta < 0$, the corresponding model with $1 > p_0 > p_1 > p_2 > p_3 > p_4 > 0$ (see top row of Fig. 5) is akin to the *anti-voter model*[36] p. 162. Finally, our set of sites $\mathbb{S}_n$ is finite and we take the limit as $n \to \infty$ in the sequel, but the set of sites in the classical voter model is the countably infinite $\mathbb{Z}^2 = \{\ldots, -2, -1, 0, 1, 2, \ldots\}^2$.

B.3 Correlated Site Percolation Model

Our model with $\beta \neq 0$ allows for correlation between the phases due to nearest-neighbor interactions. This is nearly the same as the *correlated site percolation* model of[33] Sec. C.V.3, p.131~~inspired by the classical Ising model for ferro-magnetism~~. One crucial difference is that we have thermal temperature as well as external stress in our parametrization and focus on the system behaviour under variable external stress and constant temperature for a given pair of rheological parameters α and β.

B.4 Ising Model

Our model can be reparametrized as the Ising model[29,30] with phases given by $\{-1, +1\}$ for the ferromagnetic spins due to the well-known transformation (for eg. see Problem 3, Chapter 1[38]). Despite this mathematical equivalence, one looses interpretability of yielded and unyielded states of the microscopic clumps readily available in the correlated site percolation with phases in $\{0, 1\}$.

C Algorithms

Here we present the two main algorithms for Gibbs sampling. Algorithm 1 produces a sample path in the space of site configurations under a homogeneous Markov chain with a given initial condition $x(0)$ and rheological parameters α and β, external constant stress σ and holding time h. Algorithm 2 similarly produces a sample path under an inhomogeneous Markov chain.

input :
- $x(0)$ to specify the initial distribution $\delta_{x(0)}$,
- model parameters: α, β, σ,
- average number of hits per site: h

output : a sample path $\mathbf{x} = \big(x(0), x(1), \ldots, x(\lfloor hn^2 \rfloor)\big)$ from $\{X(j)\}_{j=0}^{\lfloor hn^2 \rfloor}$ given by (4) and (5).

initialize: $j \leftarrow 0$ and $\mathbf{x} \leftarrow (x(0))$

for $j = 1, \ldots, \lfloor hn^2 \rfloor$ **do**
- $x(j) \leftarrow x(j-1)$
- pick a site s uniformly at random from $\mathbb{S}_n$
- $\theta \leftarrow \exp\big(-(\beta x_{N_s}(j) - (\sigma - \alpha))\big)$
- $u \sim \text{Uniform}(0,1)$
- **if** $u \le \frac{1}{1+\theta}$ **then** $x_s(j) \leftarrow 1$; $x_s(j) \leftarrow 0$
- $\mathbf{x}$.append$(x(j))$

end

return x

Algorithm 1: GibbsSample$(x(0), \alpha, \beta, \sigma, h)$

input :

- $x(0)$ to specify the initial distribution $\delta_{x(0)}$,
- model parameters: α, β,
- external stress function: $\sigma(m)$ for each time-block $m \in \{0,1,2,\ldots,M\}$,
- average number of hits per site per time-block m: h

output : a sample path $\mathbf{x} = \big(x(0),x(1),\ldots,x(M\lfloor hn^2 \rfloor)\big)$ from $\{X(j)\}_{j=0}^{M\lfloor hn^2 \rfloor}$ given by (8) and (7).

initialize: $m \leftarrow 0$ and $\mathbf{x} \leftarrow (x(0))$

for $m = 0,1,\ldots,M$ **do**

  for $i = 1,2,\ldots,\underline{h} = \lfloor hn^2 \rfloor$ **do**

    - $j \leftarrow m\underline{h} + i$; $\quad x(j) \leftarrow x(j-1)$
    - pick a site s uniformly at random from $\mathbb{S}_n$
    - $\theta \leftarrow \exp\left(-\left(\beta x_{N_s}(j) - (\sigma(m) - \alpha)\right)\right)$
    - $u \sim \text{Uniform}(0,1)$
    - **if** $u \leq \frac{1}{1+\theta}$ **then** $x_s(j) \leftarrow 1$; $x_s(j) \leftarrow 0$
    - $\mathbf{x}$.append$(x(j))$

  end

end

return x

Algorithm 2: IGibbsSample$(x(0),\alpha,\beta,\sigma(m),h)$

References

1 B. Y. Han, L. D. Sung and S. W. Kim, *Nature*, 1997, **388**, 860–862.

2 Y. Qiu and K. Park, *Advanced Drug Delivery Reviews*, 2001, **53**, 321 – 339.

3 Q. Hou, P. A. D. Bank and K. M. Shakesheff, *J. Matter. Chem.*, 2004, **14**, 1915.

4 J. Beck, B. Madsen, D. Britt, B. Vernon and K. T. Nguyen, *Tissue Engineering*, 2007, **13**, 589–599.

5 A. Soulies, J. Pruvost, J. Legrand, C. Castelain and T. Burghelea, *Rheologica Acta*, 2013, **52**, 589–605.

6 C. J. Dimitriou and G. H. McKinley, *Soft Matter*, 2014, **10**, 6619–6644.

7 W. H. Herschel and R. Bulkley, *Kolloid-Zeitschrift*, 1926, **39**, 291–300.

8 W. Herschel and T. Bulkley, *Am. Soc. Test Proc.*, 1926, **26(2)**, 621–633.

9 E. Bingham, *Fluidity and Plasticity*, McGraw-Hill, 1922.

10 T. C. Papanastasiou, *Journal of Rheology (1978-present)*, 1987, **31**, 385–404.

11 C. F. Möller, Peder, J. Mewis and D. Bonn, *Soft Matter*, 2006, **2**, 274–283.

12 T. Divoux, V. Grenard and S. Manneville, *Phys. Rev. Lett.*, 2013, **110**, 018304.

13 A. M. V. Putz and T. I. Burghelea, *Rheol Acta*, 2009, **48**, 673–689.

14 E. Weber, M. Moyers-Gonzalez and T. I. Burghelea, *Journal of Non-Newtonian Fluid Mechanics*, 2012, **183-184**, 14 – 24.

15 A. Poumaere, M. Moyers-GonzÃČÂąlez, C. Castelain and T. Burghelea, *Journal of Non-Newtonian Fluid Mechanics*, 2014, **205**, 28 – 40.

16 K. Dullaert and J. Mewis, *J. Non-Newtonian Fluid Mech.*, 2006, 21–30.

17 D. Quemada, *Eur. Phys. J. AP*, 1998, 119–127.

18 D. Quemada, *Eur. Phys. J. AP*, 1998, 309–320.

19 D. Quemada, *Eur. Phys. J. AP*, 1999, 191–207.

20 N. Roussel, R. Le Roy and P. Coussot, *J. non-Newtonian Fluid Mech.*, 2004, **117**, 85–95.

21 C. J. Dimitriou, R. H. Ewoldt and G. H. McKinley, *Journal of Rheology (1978-present)*, 2013, **57**, 27–70.

22 M. Moyers-Gonzalez, T. I. Burghelea and J. Mak, *Journal of Non-Newtonian Fluid Mechanics*, 2011, **166**, 515 – 531.

23 F. Bautista, M. Munoz, J. Castillo-Tejas, J. H. Pérez-López, J. E. Puig and O. Manero, *The Journal of Physical Chemistry B*, 2009, **113**, 16101–16109.

24 W. Hong, X. Zhao, J. Zhou and Z. Suo, *Journal of the Mechanics and Physics of Solids*, 2008, **56**, 1779 – 1793.

25 Y. An, F. J. Solis and H. Jiang, *Journal of the Mechanics and Physics of Solids*, 2010, **58**, 2083 – 2099.

26 J. R. de Bruyn, *Journal of Non-Newtonian Fluid Mechanics*, 2013, **193**, 21 – 27.

27 F. K. Oppong, L. Rubatat, B. J. Frisken, A. E. Bailey and J. R. de Bruyn, *Phys. Rev. E*, 2006, **73**, 041405.

28 F. K. Oppong and J. R. de Bruyn, *J. Non-Newtonian Fluid Mech.*, 2007, **142**, 104–111.

29 E. Ising, *Zeitschrift für Physik*, 1925, **31**, 253–258.

30 E. H. Stanley, *Phase transitions and critical phenomena*, Oxford University Press, 1987.

31 S. Slomkowski, J. V. Alemán, R. G. Gilbert, M. Hess, K. Horie, R. G. Jones, P. Kubisa, I. Meisel, W. Mormann, S. Penczek and R. F. T. Stepto, *Pure and Applied Chemistry*, 2011, **83**, 2229–2259.

32 R. Jones, *Compendium of polymer terminology and nomenclature IUPAC recommendations, 2008*, Royal Society of Chemistry, Cambridge, 2009.

33 D. Stauffer, A. Coniglio and M. Adam, *Advances in Polymer Science*, 1982, **44**, 103–158.

34 P. Brémaud, *Markov Chains: Gibbs Field, Monte carlo Simulation and Queues*, Springer-Verlag, New York, 1999.

35 O. Häggström, *Finite Markov Chains and Algorithmic Applications*, Cambridge University Press, 2002.

36 T. M. Liggett, *Interacting Particle Systems*, Springer Berlin Heidelberg, 1985.

37 B. Bollobás and O. Riordan, *Percolation*, Cambridge University Press, 2006.

38 M. Kardar, *Statistical Physics of Felds*, Cambridge University Press, 2007.